

MOX-Report No. 83/2026

Voronoi Depth for functional data over non-convex multidimensional supports

Cavazzutti, M.; Palummo, A.; Arnone, E.; Sun, Y.; Genton, M.G.; Sangalli, L.M.

MOX, Dipartimento di Matematica
Politecnico di Milano, Via Bonardi 9 - 20133 Milano (Italy)

mox-dmat@polimi.it https://mox.polimi.it

To appear in Journal of Multivariate Analysis 2027, 217, 105727.
Publisher's version available at https://doi.org/10.1016/j.jmva.2026.105727

Voronoi Depth for functional data over non-convex multidimensional supports

M. Cavazzutti[1], **A. Palummo**[1], **E. Arnone**[2], **Y. Sun**[3], **M. G. Genton**[3], and **L. M. Sangalli**[*1]

[1]MOX - Dept. of Mathematics, Politecnico di Milano, Milan, Italy
[2]Dept. of Management, University of Torino, Turin, Italy
[3]Statistics Program, King Abdullah University of Science and Technology, Thuwal, Saudi Arabia

4 November 2026

Abstract

In this work, we propose an integrated depth for functional data defined on non-convex multidimensional supports. Using an appropriate Voronoi tessellation of the support, the proposed method enables the analysis of functional data that are irregularly or only partially observed over the domain, with missing observations over large portions of the support. The proposed depth is consistent and inherits the statistical properties of integrated functional depths for one-dimensional supports. Through extensive simulation studies, we show that the proposed method outperforms classical approaches. Finally, we apply the proposed depth to environmental data measured on multidimensional supports. In particular, we analyze air temperatures over the Earth's surface from the CESM2 Large Ensemble Community Project and lake surface water temperatures over Lake Victoria from the ARC-Lake database. The first application involves irregularly spaced measurements, while the second illustrates the partially observed setting, highlighting the advantages of the proposed depth.

Keywords: data ranking, functional data analysis, incomplete functional data, partially observable functional data, spatial data.

1 Introduction

In this work, we propose a depth measure for functional data defined on complex multidimensional supports, such as irregular, non-convex or curved domains. In recent decades, advances in measurement technology have generated massive amounts of functional data on multidimensional domains. In the environmental sciences, satellite platforms provide global fields of key oceanographic and atmospheric indicators over the Earth's surface [see, e.g., Copernicus Programme, 2014, JPL MUR MEaSUREs Project, 2015], as well as over specific regions such as lakes and other water bodies [see, e.g., the ARC-Lake database; MacCallum and Merchant, 2011]. In the life sciences, advanced medical imaging provides biological signals measured on the surface of, or within, organs and other anatomical structures [see, e.g., Ombao et al., 2016, Arnone et al., 2023]. In many cases, the support on which these signals are observed is not only multidimensional, but may also exhibit complex geometries.

One of the main challenges in the analysis of such functional data is the lack of a natural ordering, especially when observations lie on multidimensional, non-convex supports. This hinders the definition of location and dispersion indices such as medians and quartiles, limiting the use of tools ranging from boxplots to nonparametric tests and classification rules. A natural way to address this issue is through statistical depth notions.

In recent decades, the concept of statistical depth, originally introduced for ordering multivariate data by the seminal work of Tukey [1975], has been extended to the functional setting. Fraiman and Muniz [2001] proposed the integrated functional depth, obtained by integrating a univariate depth over the domain. Projection-based depths were studied by Cuevas et al. [2007], while López-Pintado and Romo [2009] introduced the band depth and its modified version, and López-Pintado and Romo [2011] generalized the multivariate halfspace depth through the half-region depth and its modification. Other proposals include the infimal depth [Mosler, 2013], the extremal depth [Narisetty and Nair, 2016], and the functional spatial depth [Serfling and Wijesuriya, 2017].

*Correspondence: Laura.sangalli@polimi.it

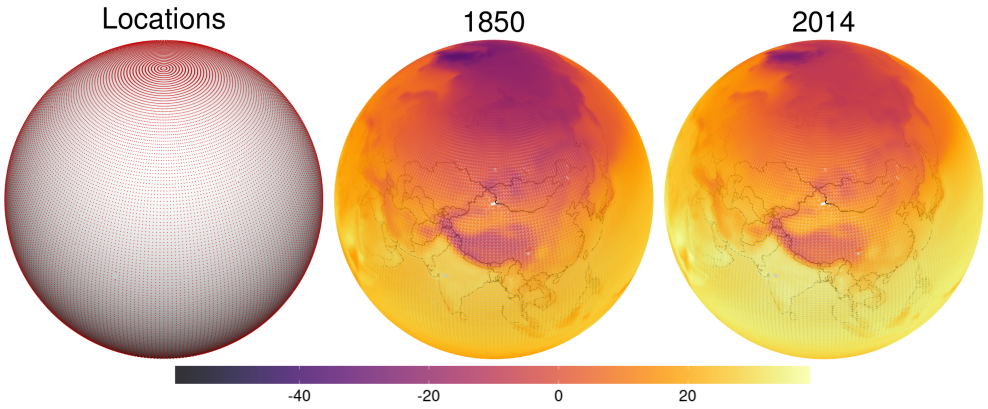

Fig. 1: Earth surface temperatures from the CESM2-LENS2 project. Left panel: measurement locations. Middle and right panels: annual mean temperatures (°C) in 1850 and 2014, respectively.

Extensions to vector-valued functional data were developed by Ieva and Paganoni [2013] and Claeskens et al. [2014]. A substantial body of work has investigated the mathematical foundations of functional depth and established an axiomatic framework [see, e.g., Chakraborty and Chaudhuri, 2014, Nieto-Reyes and Battey, 2016, Nagy et al., 2016b,a, Gijbels and Nagy, 2017]. In parallel, depth-based methods have been applied to a broad range of statistical problems, including classification, clustering [López-Pintado and Romo, 2006, Li et al., 2012], and graphical tools such as functional boxplots and related visualization techniques [see, e.g., Hyndman and Shang, 2010, Sun and Genton, 2011, 2012, Arribas-Gil and Romo, 2014, Genton et al., 2014, Dai and Genton, 2019, Ieva and Paganoni, 2020]. A recent review is provided by Qu et al. [2025].

Despite this broad literature, most functional depth notions are designed for continuously observed data on one-dimensional domains, while considerably less attention has been devoted to discretely observed functional data on multidimensional supports. Extensions to regular two-dimensional grids were proposed by Genton et al. [2014], who introduced the surface boxplot based on a volume depth for images, and by López-Pintado and Wrobel [2017], who developed robust nonparametric tests for comparing image groups using a generalized band depth. These approaches require all observations to be collected on a common regular grid, as in image data, to enable pointwise comparisons and depth computations. This assumption is often unrealistic. For example, environmental data are frequently recorded on irregular spatial grids that may differ across statistical units. A common workaround is to smooth each unit prior to depth computation, but this may introduce several drawbacks. Results can be highly sensitive to the choice of smoothing parameters, which are typically not selected for depth-based analyses, and smoothing can become computationally demanding in large-scale settings. Moreover, it is problematic when data are only partially observed, with no measurements available over large portions of the domain [see, e.g., James and Hastie, 2001, Delaigle and Hall, 2013, Kneip and Liebl, 2020, Lin et al., 2021]. Recent contributions have addressed sparse or partially observed functional data. Sguera and López-Pintado [2021] introduced a depth for sparsely observed curves, Qu and Genton [2022] proposed the sparse functional boxplot, and Elías et al. [2023] defined a depth for partially observed functional data. However, all these contributions focus on one-dimensional domains.

In this work, we introduce a depth for functional data defined on multidimensional supports, allowing for irregular and partial observation on the support. Building on Elías et al. [2023], we extend the integrated functional depth to data on multidimensional and geometrically complex domains. The proposed methodology relies on a Voronoi tessellation of the support [see, e.g., De Berg, 2000], exploiting its domain decomposition properties to obtain an effective discretization of the depth problem. We establish the main theoretical properties of the proposed depth and assess its performance through extensive simulation studies. Finally, we illustrate the methodology with two environmental applications. First, we analyze annual mean Earth surface temperatures using simulations from the CESM2 Large Ensemble Project [Rodgers et al., 2021], focusing on global surface temperature as a key climate change indicator. The data are provided on a latitude–longitude grid that is regular in geographic coordinates but irregular on the sphere, with denser sampling near the poles and sparser coverage near the equator (see Fig. 1). Second, we study lake surface water temperature in Lake Victoria, measured by satellite and available in the ARC-Lake database [MacCallum and Merchant, 2011], where observations are incomplete due to measurement limitations. The proposed methodology accommodates such irregular and partially observed data without requiring reconstruction. The implementation is based on the R/C++ library `fdaPDE` [Arnone et al., 2025].

The remainder of the paper is organized as follows. Section 2 reviews integrated functional depth and Voronoi tessellations. Section 3 introduces the proposed depth for both fully and partially observed data. Section 4

presents its theoretical properties. Section 5 reports simulation studies, while Sections 6 and 7 describe the two applications. Section 8 concludes and outlines future research directions. Technical definitions and assumptions from the literature, together with additional simulations, are reported in the Supplementary Material.

2 Framework and definitions

We consider functional data defined on a compact multidimensional support. In particular, the support S may be a (possibly non-convex) domain in $\mathbb{R}^d$, with $d \in 1, 2, 3$, or a two-dimensional Riemannian manifold embedded in $\mathbb{R}^3$, as in the application to Earth surface temperatures. We next recall the main definitions and extend them to multidimensional supports. Section 2.1 reviews the population formulation of integrated depth, together with its finite-sample counterpart. Section 2.2 recalls the definition of Voronoi tessellations, which will be used in Section 3 to develop an estimation procedure for discretely observed functional data.

2.1 *Integrated Functional Depth for multidimensional supports*

The Integrated Functional Depth (IFD), originally introduced by Fraiman and Muniz [2001] for one-dimensional supports, can be naturally extended to functional data defined on non-convex multidimensional supports. By integrating a pointwise depth on the domain, it naturally accounts for the geometry of the support.

Let Γ denote the collection of all probability measures on $(\mathbb{R}, \mathcal{B}(\mathbb{R}))$, where $\mathcal{B}(\mathbb{R})$ is the Borel σ-algebra on $\mathbb{R}$. Let also $D : \mathbb{R} \times \Gamma \to [0, 1]$ be a univariate depth satisfying properties D1–D7 of Nagy et al. [2016b]. These are standard desirable properties satisfied by many commonly used univariate depths, including the Simplicial Depth [Liu, 1990] employed in Section 5. For completeness, the properties are reported in Section S1 of the Supplementary Material. Consider a stochastic process $X : S \to \mathbb{R}$, with law P, and denote by $P_{\boldsymbol{s}}$, for $\boldsymbol{s} \in S$, the marginal distribution for $X(\boldsymbol{s})$. We assume $X \in \mathcal{C}(S)$, where $\mathcal{C}(S)$ is the space of continuous functions over S. We here focus on a generalization of the IFD that involves a weight, as introduced by Claeskens et al. [2014]. We point out that for specific choices of the univariate depth integrand D, this weighted depth includes as special cases the Modified Band Depth [López-Pintado and Romo, 2009], the Modified Epigraph Depth and the Modified Hypograph Depth [López-Pintado and Romo, 2011]. Specifically, let $w : S \to \mathbb{R}^+$ be a positive weight function such that $\int_S w(\boldsymbol{s})\mathrm{d}\boldsymbol{s} = 1$ with respect to the Lebesgue measure. In this manuscript, the weight w is used in Section 3.1 to handle partially observed functional data. More generally, however, it can incorporate prior information on the phenomenon of interest by reweighting univariate depths over different portions of the support S. As an example, one may consider a step weight assigning a higher weight to either sea or land areas in environmental applications; see Claeskens et al. [2014] for admissible choices. The Integrated Functional Depth of $x \in \mathcal{C}(S)$ with respect to P is defined as

$$\mathrm{IFD}(x, P) = \int_S D(x(\boldsymbol{s}), P_{\boldsymbol{s}})\, w(\boldsymbol{s})\, \mathrm{d}\boldsymbol{s}. \tag{1}$$

In practice, the law P of the stochastic process X is unknown and must be estimated from data. Let $X_1, \ldots, X_n$ be n i.i.d. realizations of X. Denote by P_n the corresponding empirical distribution, which assigns equal weight to each functional datum, and by $P_{\boldsymbol{s},n}$ the empirical distribution of the observed univariate sample at $\boldsymbol{s}$, $\{X_i(\boldsymbol{s})\}_{i\in\{1,\ldots,n\}}$. By replacing P and $P_{\boldsymbol{s}}$ in eq. (1) with P_n and $P_{\boldsymbol{s},n}$, respectively, we obtain the sample version of the IFD, denoted by $\mathrm{IFD}_n(x)$, given by

$$\mathrm{IFD}_n(x) = \mathrm{IFD}(x, P_n) = \int_S D(x(\boldsymbol{s}), P_{\boldsymbol{s},n})\, w(\boldsymbol{s})\, \mathrm{d}\boldsymbol{s}. \tag{2}$$

The definition of IFD_n in eq. (2) assumes that the functional data are observed continuously at any point $\boldsymbol{s} \in S$. In practice, however, functional data are observed on a discrete set of locations and are often corrupted by noise. Therefore, the integral in eq. (2) must be approximated using discrete and noisy realizations of the data, possibly measured on different observation grids across statistical units. In the literature on functional data defined over one-dimensional supports, the integral in eq. (2) is often replaced by a discrete sum over the available locations, implicitly assuming that the observation grid is common across statistical units and evenly spaced [see, e.g., Claeskens et al., 2014, Nagy et al., 2016b]. Genton et al. [2014], López-Pintado and Wrobel [2017] consider functional data defined over regular multidimensional supports, also assuming that the data are measured on a common regular grid. However, when observations are unevenly distributed over the support, this approach may substantially overweight, in the depth computation, those regions where measurements are denser. In the application to Earth surface temperatures, for instance, the behavior of the functional data near the poles, where the observation grid is finer, would receive greater weight than that near the equator, where the grid is coarser. Moreover, the observation grid may vary across statistical units, and, for some units, the

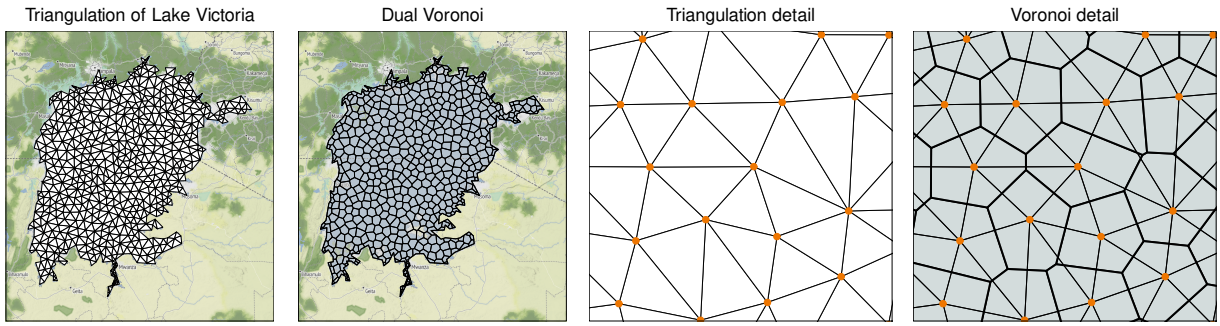

Fig. 2: Example of a Delaunay triangulation of the Lake Victoria domain and the corresponding dual Voronoi tessellation. The right panels show details of the two geometric structures.

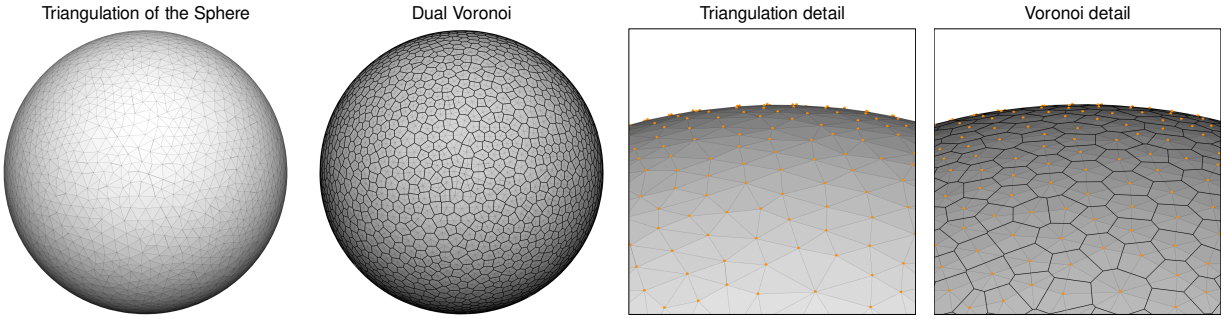

Fig. 3: Example of Delaunay triangulation of the spherical surface and the corresponding dual Voronoi tessellation, with details of the two geometrical structures on the right.

functional data may be entirely missing over large portions of the support. To address these issues, we propose a discretization of the IFD_n based on a Voronoi tessellation of the spatial support S. The next section briefly reviews Voronoi tessellations.

2.2 *Voronoi tessellation*

A Voronoi tessellation of the domain $S \subset \mathbb{R}^d$, $d \geq 1$, is the geometric partition of S into subregions, or cells, based on the distance from a set of points, $\{\boldsymbol{\xi}_1, \ldots, \boldsymbol{\xi}_K\} \subset S$ called seeds, where K denotes the number of seeds. Each cell E_k is a subset of S (or a discretization of S in the case of manifold domains) that contains all points closer to its defining seed $\boldsymbol{\xi}_k$ than to any other seed, that is $E_k := \{\boldsymbol{s} \in S | d_S(\boldsymbol{s}, \boldsymbol{\xi}_k) < d_S(\boldsymbol{s}, \boldsymbol{\xi}_h), \forall h \in \{1, \ldots, K\}, h \neq k\}$, where d_S denotes the natural metric of the domain, such as the Euclidean distance restricted to S for planar or three-dimensional domains or the geodesic distance for surface domains. A Voronoi tessellation of S can be obtained as the dual of a constrained Delaunay triangulation of S [see, e.g., De Berg, 2000]. Delaunay triangulations are well-known geometric structures that can be computed efficiently [see, e.g., Hjelle and Dæhlen, 2006]. Their vertices define the seeds of the corresponding Voronoi tessellation. Fig. 2 shows an example of a constrained Delaunay triangulation and the associated Voronoi tessellation of Lake Victoria, the support of the functional data presented in Section 7. The right panels show details of the tessellation. Fig. 3 shows a similar construction for the spherical surface, the support of the functional data presented in Section 6.

Let $\mathcal{T}(S, \boldsymbol{\xi})$ denote the Delaunay triangulation of S and let $S_{\mathcal{T}}$ be the corresponding discretized domain, defined as the union of the simplices in $\mathcal{T}(S, \boldsymbol{\xi})$. For planar domains with polygonal boundaries, $S_{\mathcal{T}} = S$; for curved domains, $S_{\mathcal{T}}$ is a piecewise-linear approximation of S; see Fig. 3. The dual Voronoi tessellation is denoted by $\mathcal{V}(S_{\mathcal{T}}, \boldsymbol{\xi})$; it is generated by the same seeds $\{\boldsymbol{\xi}_k\}_{k=1}^K$ and partitions $S_{\mathcal{T}}$ into cells $\{E_k\}_{k=1}^K$. Let λ be the Lebesgue measure on S. We write $\Pi_{S_{\mathcal{T}}} : S \to S_{\mathcal{T}}$ for the projection onto the discretized domain, so that $\boldsymbol{s}_{\mathcal{T}} = \Pi_{S_{\mathcal{T}}}(\boldsymbol{s})$ for any $\boldsymbol{s} \in S$, and $\Pi_{S_{\mathcal{T}}}(\boldsymbol{\xi}_k) = \boldsymbol{\xi}_k$ for all $k \in \{1, \ldots, K\}$. We denote by $\lambda_{\mathcal{T}}(E_k) > 0$ the restricted Lebesgue measure of E_k, that is $\lambda_{\mathcal{T}}(E_k) = \lambda(\Pi_{S_{\mathcal{T}}}^{-1}(E_k))$, where $\Pi_{S_{\mathcal{T}}}^{-1}(E_k)$ is the preimage of E_k under $\Pi_{S_{\mathcal{T}}}$. Then, up to a set of zero restricted measure, $S_{\mathcal{T}} = \bigcup_{k \in \{1,\ldots,K\}} E_k$. In the remainder, we write $\mathcal{T}$ for $\mathcal{T}(S, \boldsymbol{\xi})$ and $\mathcal{V}$ for $\mathcal{V}(S_{\mathcal{T}}, \boldsymbol{\xi})$.

3 Voronoi Depth

We now introduce the proposed depth measure. Section 3.1 presents the Voronoi Depth, a discretization of the Integrated Functional Depth for discretely observed data. Section 3.2 then extends the proposed depth to partially observed functional data.

3.1 *Voronoi Depth*

Let $X_1, \ldots, X_n$ be the sample of functional data, discretely observed over possibly different observational grids, where the i-th statistical unit X_i, namely the i-th functional observation, is measured at locations $\{\boldsymbol{s}_{i,j}\}_{j\in\{1,\ldots,m_i\}}$ so that the sample is given by $\{X_i(\boldsymbol{s}_{i,j})\}_{j\in\{1,\ldots,m_i\};i\in\{1,\ldots,n\}}$, where m_i is the number of discrete measurements for X_i. Let also $\{x(\boldsymbol{s}_j)\}_{j\in\{1,\ldots,m_x\}}$ be the discretely observed version of a general function $x : S \to \mathbb{R}$, with m_x discrete measurements. In this section, although observational grids may differ across statistical units, we assume that each statistical unit is, in principle, observable over any portion of the domain S. Specifically, we assume that for each statistical unit i and each Voronoi cell E_k of the Voronoi tessellation $\mathcal{V}$ of S there is at least one $\boldsymbol{s}_{i,j}$ such that its projection on $S_\mathcal{T}$ is in E_k, i.e. $(\boldsymbol{s}_{i,j})_\mathcal{T} \in E_k$. The next section relaxes this assumption and considers partially observed functional data.

We are now ready to define the Voronoi Depth for irregularly measured functions.

Definition 1 (Voronoi Depth)**.** Consider the discretely observed functional sample $\{X_i(\boldsymbol{s}_{i,j})\}_{j\in\{1,\ldots,m_i\};\, i\in\{1,\ldots,n\}}$ defined on the support S, and the Voronoi tessellation $\mathcal{V}$ of S. The Voronoi Depth (VD) of a function $x \in \mathcal{C}(S)$, measured at locations $\{\boldsymbol{s}_j\}_{j\in\{1,\ldots,m_x\}}$, is defined as

$$\mathrm{VD}(x) := \sum_{k=1}^{K} D(x_\mathcal{V}(\boldsymbol{\xi}_k), P_{\boldsymbol{\xi}_k,n,\mathcal{V}})w(\boldsymbol{\xi}_k)\lambda_\mathcal{T}(E_k), \tag{3}$$

where, for every $\boldsymbol{s} \in S$,

$$x_\mathcal{V}(\boldsymbol{s}) = \sum_{k=1}^{K} \frac{\sum_{j=1}^{m_x} \mathbb{I}_{E_k}((\boldsymbol{s}_j)_\mathcal{T})\, x(\boldsymbol{s}_j)}{\sum_{j=1}^{m_x} \mathbb{I}_{E_k}((\boldsymbol{s}_j)_\mathcal{T})} \mathbb{I}_{E_k}(\boldsymbol{s}_\mathcal{T}); \qquad P_{\boldsymbol{s},n,\mathcal{V}} = \frac{1}{n}\sum_{i=1}^{n} X_{i,\mathcal{V}}(\boldsymbol{s})\delta_{X_{i,\mathcal{V}}(\boldsymbol{s})},$$

with $\delta_{X_{i,\mathcal{V}}(\boldsymbol{s})}$ the Dirac's delta in $X_{i,\mathcal{V}}(\boldsymbol{s})$, where $X_{i,\mathcal{V}}$ is defined analogously to $x_\mathcal{V}$ for the functions X_i, $i \in \{1, \ldots, n\}$.

The proposed Voronoi Depth is a discrete approximation of the Integrated Functional Depth based on a Voronoi tessellation of S. Its computation does not require the observational grid to be common across statistical units, nor that it be evenly spaced. Each functional datum contributes to the depth through the average of its measurements within each Voronoi cell, yielding a piecewise-constant representation of the functional data over the tessellation. The resulting discretization adapts to the geometry of the support and enables accurate numerical integration.

Finally, the computational cost of the proposed VD is generally lower than that of classical approaches. The cost of computing a Voronoi tessellation in the present setting is $O(K\log(K))$ once a Delaunay triangulation of the support is available [Hjelle and Dæhlen, 2006]. Moreover, the tessellation only needs to be computed once for all functional observations sharing the support S. The dominant computational cost of the VD arises from ranking the univariate evaluations of the functional data at the Voronoi seeds $\boldsymbol{\xi}_k$, resulting in a complexity of $O(Kn^2)$. By contrast, existing alternatives for two-dimensional domains have computational complexity $O(mn^2)$, where m denotes the size of the observational grid [see, Genton et al., 2014, López-Pintado and Wrobel, 2017].

3.2 *Voronoi Depth for Partially Observed functional data*

We now extend the proposed VD to deal with partially observable functional data. Such data, also known as incomplete functional data, functional fragments, or functional snippets [Lin et al., 2021], are frequently encountered in applications and have recently attracted considerable attention; see, e.g., the review by Elías et al. [2023]. Specifically, we generalize the IFD in eq. (1) and the VD in eq. (3) to accommodate partially observable functional data, building on the work of Elías et al. [2023], who introduced a functional depth for one-dimensional domains in the partial observability framework of Delaigle and Hall [2013].

Consider a random observational mechanism Q that generates compact sets $O \subset S$ with positive Lebesgue measure. Let $Q(\boldsymbol{s}) = \Pr(O \ni \boldsymbol{s})$, and suppose that X is observable only on the subset O of S. In this manuscript, we adopt the regularity conditions A1–A3 on the observational process introduced by Elías et al. [2023]. Without loss of generality, these conditions imply that $Q(\boldsymbol{s}) > 0$, $\forall \boldsymbol{s} \in S$. Moreover, condition A3 corresponds to the standard Missing-Completely-at-Random (MCAR) mechanism [see, e.g., Kraus, 2014, Kneip

and Liebl, 2020], meaning that the observational process does not depend on the value of the function. This assumption is standard in the literature on partially observed functional data. Simulation evidence in Elías and Nagy [2025] suggests that moderate departures from MCAR have limited impact on the definition of depths for partially observed data.

The functional depth for partially observed functional data, introduced by Elías et al. [2023] and further studied by Elías and Nagy [2025], can be naturally extended to functional data observed over multidimensional supports. Consider the pair $(x, o) \in \mathcal{C}(o) \times \mathcal{P}(S)$, where $\mathcal{P}(S) := \{O \subset S | O \text{ is compact}\}$. The depth associated with the pair (x, o) is obtained through a suitable weight function w that depends on the observability process. Let $\phi : [0, 1] \to [0, 1]$ be a continuous function such that $\int_O \phi(Q(\boldsymbol{s}))\, \mathrm{d}\boldsymbol{s} > 0$ almost surely, and define the restriction of the weighting function w to the compact set O:

$$w_\phi(\boldsymbol{s}|O) = \frac{\phi(Q(\boldsymbol{s}))}{\int_O \phi(Q(\boldsymbol{z}))\, \mathrm{d}\boldsymbol{z}}, \qquad \forall \boldsymbol{s} \in O.$$

The function ϕ determines how the observability process Q affects the weighting function. In this manuscript, we adopt the identity function on $[0, 1]$ as the default choice for ϕ, thereby assigning greater weight to regions with higher observability and reducing the influence of sparsely observed regions. Alternative choices are possible, allowing different weighting schemes depending on the application, as discussed in Elías and Nagy [2025]. We can now define the Partially Observed Integrated Functional Depth

$$\mathrm{POIFD}((x, o), P \times Q) = \int_o D(x(\boldsymbol{s}), P_{\boldsymbol{s}})\, w_\phi(\boldsymbol{s}|o)\, \mathrm{d}\boldsymbol{s},$$

that generalizes the IFD in eq. (1) to functions partially observed on multidimensional supports.

Now let $O_1, \ldots, O_n$ be n i.i.d. realizations of O, with X_i continuously observed on O_i, for $i \in \{1, \ldots, n\}$. The pairs $(X_1, O_1), \ldots, (X_n, O_n)$ are independent and identically distributed under the MCAR assumption. Let $I(\boldsymbol{s}) = \{i \in \{1, \ldots, n\} : \boldsymbol{s} \in O_i\}$. The empirical estimate Q_n of Q is defined as $Q_n(\boldsymbol{s}) = \frac{1}{n}|I(\boldsymbol{s})|$, $\forall \boldsymbol{s} \in S$, where $|\cdot|$ denotes the cardinality of a set. Replacing Q and P in the POIFD definition with their empirical estimates Q_n and P_n yields the sample counterpart of eq. (2) for partially observable functional data:

$$\mathrm{POIFD}_n(x, o) = \mathrm{POIFD}((x, o), P_n \times Q_n) = \int_o D(x(\boldsymbol{s}), P_{\boldsymbol{s},n})\, w_{\phi,n}(\boldsymbol{s}|o)\, \mathrm{d}\boldsymbol{s}, \tag{4}$$

where

$$w_{\phi,n}(\boldsymbol{s}|o) = \frac{\phi(Q_n(\boldsymbol{s}))}{\int_o \phi(Q_n(\boldsymbol{z}))\, \mathrm{d}\boldsymbol{z}}.$$

To simplify notation, we use $\mathrm{POIFD}_n(x, o)$ instead of $\mathrm{POIFD}((x, o), P_n \times Q_n)$ in the remainder of the paper.

Consider now discretely observed functional data $\{X_i\}_{i\in\{1,\ldots,n\}}$, as in Section 3.1, but without the simplifying assumption that the functions are observable over the whole domain S. We then need to discretize Q_n and approximate the integral in eq. (4), based on pointwise observations of X_i. Let $\mathbb{I}_{O_{i,\mathcal{V}}}$ denote the indicator function of $O_{i,\mathcal{V}}$, where $O_{i,\mathcal{V}}$ is the Voronoi representation of O defined as

$$O_{i,\mathcal{V}} = \bigcup_{\substack{k\in\{1,\ldots,K\} \\ \exists j:(\boldsymbol{s}_{i,j})_{\mathcal{T}} \in E_k}} E_k.$$

We can now define the Partially Observed Voronoi Depth (POVD) as the discrete counterpart of the POIFD in (4) for discretely observed functional data.

Definition 2 (Partially Observed Voronoi Depth)**.** Given the Voronoi discretization $\mathcal{V}$ of the support S and the discretely observed functional sample $(\{X_1(\boldsymbol{s}_{1,j})\}_{j\in\{1,\ldots,m_1\}}, O_{1,\mathcal{V}}), \ldots, (\{X_n(\boldsymbol{s}_{n,j})\}_{j\in\{1,\ldots,m_n\}}, O_{n,\mathcal{V}})$, the Voronoi Depth for Partially Observed Data is

$$\mathrm{POVD}(x, o) = \sum_{\substack{k\in\{1,\ldots,K\} \\ E_k \subset o_{\mathcal{V}}}} D(x_{\mathcal{V}}(\boldsymbol{\xi}_k), P_{\boldsymbol{\xi}_k,n,\mathcal{V}})\, w_{\phi,n}(\boldsymbol{\xi}_k|o_{\mathcal{V}})\, \lambda_{\mathcal{T}}(E_k),$$

where $x_{\mathcal{V}}(\boldsymbol{\xi}_k)$ and $X_{i,\mathcal{V}}(\boldsymbol{\xi}_k)$ are defined as in Definition 1, and $P_{\boldsymbol{\xi}_k,n,\mathcal{V}}$ is the empirical distribution of $X_{i,\mathcal{V}}(\boldsymbol{\xi}_k)$ for all i for which there exists at least one spatial measurement $\boldsymbol{s}_{i,j}$ such that $(\boldsymbol{s}_{i,j})_{\mathcal{T}} \in E_k$.

Note that POVD is computed from a number of observed Voronoi cells that may vary across statistical units, potentially affecting its variability. The weighting function w_ϕ mitigates this effect by assigning greater weight to highly observed regions. A simulation study in Section S2 of the Supplementary Material illustrates this behavior.

4 Theoretical properties of Voronoi Depth

This section investigates the theoretical properties of the proposed Voronoi Depth. Since the VD in Definition 1 is a special case of the POVD in Definition 2 when $O = S$, we focus on the latter, noting that all results directly apply to the VD.

Before studying the asymptotic properties of the proposed POVD, we establish the large-sample behavior of the empirical POIFD_n defined in eq. (4). The corresponding results for one-dimensional domains were established by Elías and Nagy [2025], leveraging the results of [Nagy et al., 2016b]; the following propositions extend them to multidimensional supports under analogous assumptions.

Proposition 1 (Strong consistency)**.** *Under the strong consistency of the univariate depth D (i.e., condition C1 in Section S1 of the Supplementary Material) the empirical* POIFD *is strongly consistent; that is, for any fixed (x, o):*

$$\text{POIFD}_n(x, o) \xrightarrow[n\to\infty]{a.s.} \text{POIFD}(x, o).$$

Proof: The proof follows that of Theorem 5 in [Elías and Nagy, 2025]. In particular, by the strong consistency of D, the continuity of ϕ, and the MCAR assumption, we obtain

$$D\big(x(\mathbf{s}); P_{n,\mathbf{s}}\big)\phi(Q_n(\boldsymbol{s})) \xrightarrow[n\to\infty]{a.s.} D\big(x(\mathbf{s}); P_{\mathbf{s}}\big)\phi(Q(\boldsymbol{s})) \qquad \text{for all } \mathbf{s} \in o.$$

Since ϕ and D are bounded and λ is the Lebesgue measure on the compact set S, the dominated convergence theorem applies, yielding, $\forall\, x, o$,

$$\int_o D\big(x(\mathbf{s}); P_{n,\mathbf{s}}\big)\phi(Q_n(\boldsymbol{s}))\mathrm{d}\boldsymbol{s} \xrightarrow[n\to\infty]{a.s.} \int_o D\big(x(\mathbf{s}); P_{\mathbf{s}}\big)\phi(Q(\boldsymbol{s}))\mathrm{d}\boldsymbol{s},$$

and

$$\int_o \phi(Q_n(\boldsymbol{s}))\mathrm{d}\boldsymbol{s} \xrightarrow[n\to\infty]{a.s.} \int_o \phi(Q(\boldsymbol{s}))\mathrm{d}\boldsymbol{s}.$$

Finally, since $\int_o \phi(Q(\boldsymbol{s})) > 0$ almost surely, the result follows from the definition of POIFD_n and the continuous mapping theorem. □

In order to extend the strong uniform consistency and weak continuity of the POIFD to functional data over multidimensional supports S, we require the following assumption A1 in place of condition C3 of Elías and Nagy [2025]:

A1: O is almost surely a finite union of compact sets and satisfies $\Pr(\boldsymbol{s} \in O) = \Pr(\boldsymbol{s} \in \text{interior of } O)$.

Proposition 2 (Strong uniform consistency and weak continuity)**.** *Assume that condition A1 holds.*

1. *Under the uniform consistency of the depth D (condition C2 of the Supplementary Material) , for any $G > 0$:*

$$\sup_{\substack{o\subset S,\ x\in\mathcal{C}(S)\\ \lambda(o)\geq G}} |\text{POIFD}_n(x, o) - \text{POIFD}(x, o)| \xrightarrow[n\to\infty]{a.s.} 0.$$

2. *Under the weak continuity of the depth D (condition C3 of the Supplementary Material) , for any sequence of probability measures $\{P_\gamma\}_{\gamma\in\{1,\dots,\infty\}}$ converging weakly to P, and for any constant $G > 0$, we have:*

$$\sup_{\substack{o\subset S,\ x\in\mathcal{C}(S)\\ \lambda(o)\geq G}} |\text{POIFD}_\gamma(x, o) - \text{POIFD}(x, o)| \xrightarrow[\gamma\to\infty]{} 0,$$

where $\text{POIFD}_\gamma(x, o)$ denotes the POIFD *of x observed over the set o, with respect to the product measure $P_\gamma \times Q$.*

Proof: The proof follows the derivation of Theorem 6 and 8 in Elías and Nagy [2025], with $[0, 1]$ replaced by the support $S \subset \mathbb{R}^d$. In particular, notice that Lemma 7 of the same manuscript holds independently of the dimensionality of S. Therefore, using Proposition 1, the proof reduces to establishing that:

$$\sup_{\boldsymbol{s}\in S} |\phi(Q_n(\boldsymbol{s})) - \phi(Q(\boldsymbol{s}))| \xrightarrow[n\to\infty]{a.s.} 0.$$

Under condition A1, we can apply the Glivenko-Cantelli theorem for the capacity functional of the random set $O \subset S$ [theorem 5.6 in Molchanov and Molinari, 2018], and thus $\sup_{\boldsymbol{s}\in S} |Q_n(\boldsymbol{s}) - Q(\boldsymbol{s})| \xrightarrow[n\to\infty]{a.s.} 0$. Since ϕ is continuous on a compact domain, it is uniformly continuous, and the result follows. □

We now turn to the consistency of the proposed Voronoi Depth, that is, the depth for discretely observed functional data. In this setting, each function X_i is observed at a finite number of locations m_i, introducing a second asymptotic regime in addition to the sample size n. Specifically, consistency requires considering both $m_i \to \infty$, corresponding to increasingly dense observations of each pair (X_i, O_i) while keeping n fixed, and $n \to \infty$, ensuring that the sample eventually captures the joint distribution of (X, O). Let m denote the minimum of the m_i. We now establish the consistency of the POVD as both m and n tend to infinity.

For each Voronoi cell E_k, let m_i^k be the number of observations of X_i in cell E_k, namely $m_i^k = \sum_{j=1}^{m_i} \mathbb{I}_{E_k}((\boldsymbol{s}_{i,j})_{\mathcal{T}})$. Let also $\nu_k := \min\{r > 0 : E_k \subset B_r(\boldsymbol{\xi}_k)\}$, where $B_r(\boldsymbol{\xi}_k)$ denotes the Euclidean ball of radius r centered at $\boldsymbol{\xi}_k$ in $\mathbb{R}^d$; when S is a two-dimensional manifold, the ball is taken in $\mathbb{R}^3$. Moreover, let $\nu = \max_{k\in\{1,\dots,K\}}\{\nu_k\}$. In what follows, we assume that Voronoi tessellations depend on the minimum number of available observations m. As m increases, a finer tessellation is considered to capture finer details in the data. More precisely, we assume the following conditions on the Voronoi tessellation:

V1 : $K \xrightarrow[m\to\infty]{} \infty$.

V2 : $\nu \xrightarrow[m\to\infty]{} 0$.

V3 : $m_i^k \xrightarrow[m\to\infty]{} \infty$ for all $k \in \{1, \dots, K\}$ and $i \in \{1, \dots, n\}$.

V4 : for all compact subsets $O \subset S$ and their Voronoi representation $O_{\mathcal{V}}$, $d_h(O, O_{\mathcal{V}}) \xrightarrow[K\to\infty]{} 0$, where $d_h(\cdot,\cdot)$ is the Hausdorff distance.

Conditions V1 and V2 require the tessellation to become increasingly refined as the number of available observations grows. Condition V3 ensures that the number of observations within each Voronoi cell diverges in the limit. Therefore, the refinement of the tessellation cannot be too fast with respect to the increase of m. In particular, V3 implies that $m/K \to \infty$ as $m \to \infty$. Finally, V4 is a standard regularity condition ensuring the asymptotic consistency of the Voronoi tessellation and the underlying Delaunay triangulation [see, e.g., Quarteroni and Valli, 1999]. In particular, it implies that $\boldsymbol{s}_{\mathcal{T}} \xrightarrow[K\to\infty]{} \boldsymbol{s}$ for all $\boldsymbol{s} \in S$.

To establish the consistency of the proposed POVD, we first prove an intermediate result on the pointwise convergence of $x_{\mathcal{V}}$ to x.

Lemma 1. *Assume that conditions V1–V4 hold. Then, for any continuous function $x : o \to \mathbb{R}$ defined on $o \subset S$,*

$$x_{\mathcal{V}}(\boldsymbol{s}) \xrightarrow[m\to\infty]{} x(\boldsymbol{s}) \quad a.s. \quad \forall \boldsymbol{s} \in o, \tag{5}$$

where $x_{\mathcal{V}}$ is defined in Definition 1.

Proof: For any $\boldsymbol{s} \in o$, let $k^\star$ be such that $\boldsymbol{s}_{\mathcal{T}} \in E_{k^\star}$. Both $k^\star$ and $E_{k^\star}$ depend on K, but this dependence is omitted for notational simplicity. From the definition of $x_{\mathcal{V}}$,

$$x_{\mathcal{V}}(\boldsymbol{s}) = \frac{1}{m_x^{k^\star}} \sum_{j=1}^{m_x} x(\boldsymbol{s}_j)\mathbb{I}_{E_k^\star}((\boldsymbol{s}_j)_{\mathcal{T}}).$$

Since x is continuous on o, it is integrable over $\Pi_{\mathcal{T}}^{-1}(E_{k^\star})$. By condition V3, as $m \to \infty$, $x_{\mathcal{V}}(\boldsymbol{s})$ converges to the Monte Carlo approximation of the integral [Owen, 2013], that is,

$$\lim_{m\to\infty} x_{\mathcal{V}}(\boldsymbol{s}) = \lim_{m_x^{k^\star}\to\infty} \frac{1}{m_x^{k^\star}} \sum_{j=1}^{m_x} x(\boldsymbol{s}_j)\mathbb{I}_{E_k^\star}((\boldsymbol{s}_j)_{\mathcal{T}}) = \frac{1}{\lambda_{\mathcal{T}}(E_{k^\star})} \int_{\Pi_{\mathcal{T}}^{-1}(E_{k^\star})} x(\boldsymbol{s})\mathrm{d}\boldsymbol{s} \quad a.s.. \tag{6}$$

By the integral mean value theorem [see, e.g., Stewart, 2015], there exists $\boldsymbol{\eta}_K \in \Pi_{\mathcal{T}}^{-1}(E_{k^\star})$ such that the right-hand side of (6) equals $x(\boldsymbol{\eta}_K)$. Moreover, by V1 and V2, we have $\lim_{m\to\infty}\|\boldsymbol{s} - \boldsymbol{\eta}_K\| = \lim_{K\to\infty}\|\boldsymbol{s} - \boldsymbol{\eta}_K\| = 0$, where $\|\cdot\|$ denotes the Euclidean norm in $\mathbb{R}^d$. Hence, by the continuity of x, assumptions V1 and V4, and (6), we obtain eq. (5). □

Using Lemma 1, we establish the consistency of the POVD in Definition 2 under the regularity conditions stated above.

Theorem 1. *Under assumptions V1–V4, for any constant $G > 0$,*

$$\sup_{\substack{o\subset S,\ x\in\mathcal{C}(S)\\ \lambda(o)\geq G}} |\mathrm{POVD}(x, o) - \mathrm{POIFD}(x, o)| \xrightarrow[\substack{m\to\infty\\ n\to\infty}]{} 0 \quad a.s.$$

Proof: Let $P_{\boldsymbol{s},n,\mathcal{V}}$ denote the empirical marginal distribution of X, defined by

$$P_{\boldsymbol{s},n,\mathcal{V}} = \frac{\sum_{i=1}^{n} \mathbb{I}_{O_{i,\mathcal{V}}}(\boldsymbol{s}_{\mathcal{T}}) X_{i,\mathcal{V}}(\boldsymbol{s}) \delta_{X_{i,\mathcal{V}}(\boldsymbol{s})}}{\sum_{i=1}^{n} \mathbb{I}_{O_{i,\mathcal{V}}}(\boldsymbol{s}_{\mathcal{T}})}.$$

We first establish the weak convergence of the marginals $P_{\boldsymbol{s},n,\mathcal{V}}$ to $P_{\boldsymbol{s}}$ for any $\boldsymbol{s} \in S$. Since almost sure convergence implies convergence in probability [see, e.g., Theorem 2.1 in Billingsley, 1999], Lemma 1 implies that the distribution of $X_{i,\mathcal{V}}(\boldsymbol{s})$ converges weakly to that of $X_i(\boldsymbol{s})$ as $m \to \infty$, for $i \in \{1, \ldots, n\}$. Letting $n \to \infty$, and recalling that $Q(\boldsymbol{s}) > 0$ a.s. for every $\boldsymbol{s} \in S$, the random variables $\{X_i(\boldsymbol{s})\}_{i \in \{1,\ldots,n\}}$ are i.i.d. with common distribution $P_{\boldsymbol{s}}$. Therefore, by the Glivenko–Cantelli theorem, the empirical marginal distributions converge weakly to $P_{\boldsymbol{s}}$. The remainder of the proof follows the arguments used in the proof of Theorem 9 of Elías and Nagy [2025]. □

5 Simulation studies

In the functional depth literature, new depths are often assessed through their ability to distinguish between data generated by different stochastic processes [see, e.g., Fraiman and Muniz, 2001, López-Pintado and Romo, 2009, 2011, Claeskens et al., 2014, Ieva and Paganoni, 2020, among others]. Accordingly, we investigate the ability of the proposed depths to discriminate between different populations. Additional simulation studies assessing the POVD's robustness to partial observability and its sensitivity to Voronoi tessellation refinement are reported in the Supplementary Material.

Let S be the unit sphere. Data are generated from the four models defined below.

M0 (baseline model): $X^{\mathrm{M0}}(\boldsymbol{s}) : S \to \mathbb{R}$ is a Gaussian process with zero mean and Matérn covariance

$$C_{\boldsymbol{\delta}}(\boldsymbol{h}) = \frac{2^{1-0.45}}{\Gamma(0.45)} (\sqrt{0.9} \frac{\|\boldsymbol{h}\|_2}{2})^{0.45} K_{0.45}(\sqrt{0.9} \frac{\|\boldsymbol{h}\|_2}{2}), \qquad \boldsymbol{h} \in \mathbb{R}^3,$$

where K_ν denotes the Bessel function of the second kind with parameter $\nu = 0.45$.

M1 (magnitude model): $X^{\mathrm{M1}}(\boldsymbol{s}) : S \to \mathbb{R}$ is defined as

$$X^{\mathrm{M1}}(\boldsymbol{s}) = X^{\mathrm{M0}}(\boldsymbol{s}) + \gamma 0.5 \mathbb{I}_{[a,a+40]\times[b,b+40]}(\zeta(\boldsymbol{s})),$$

where $\gamma \sim Bern(0.5)$, $\zeta : S \to S_{planar} = [-180, 180] \times [-90, 90]$ maps $\boldsymbol{s} \in S$ to its longitude–latitude coordinates, and (a, b) is a random longitude–latitude pair uniformly distributed over S_{planar}.

M2 (covariance model): $X^{\mathrm{M2}}(\boldsymbol{s}) : S \to \mathbb{R}$ is defined as

$$X^{\mathrm{M2}}(\boldsymbol{s}) = X^{\mathrm{M0}}(\boldsymbol{s}) \mathbb{I}_{[-180,180]\times[-50,50]}(\zeta(\boldsymbol{s})) + \delta(\boldsymbol{s}) \mathbb{I}_{[-180,180]\times([-90,-50]\bigcup[50,90])}(\zeta(\boldsymbol{s})),$$

where $\delta(\boldsymbol{s})$ is a Gaussian process with zero mean and Matérn covariance

$$C_{\boldsymbol{\delta}}(\boldsymbol{h}) = \frac{2^{1-0.45}}{\Gamma(0.45)} (\sqrt{0.9} \frac{\|\boldsymbol{h}\|_2}{4})^{0.45} K_{0.45}(\sqrt{0.9} \frac{\|\boldsymbol{h}\|_2}{4}), \qquad \boldsymbol{h} \in \mathbb{R}^3.$$

M3 (shape model): $X^{\mathrm{M3}}(\boldsymbol{s}) : S \to \mathbb{R}$ is defined as

$$X^{\mathrm{M3}}(\boldsymbol{s}) = X^{\mathrm{M0}}(\boldsymbol{s}) + f(\zeta(\boldsymbol{s})),$$

where $f(\mathrm{lon},\mathrm{lat}) = 0.1 * \sin(4\pi \mathrm{lat}/180) + 0.1 * \cos(4\pi \mathrm{lat}/180)$, where lon and lat denote the longitude and latitude coordinates of $\boldsymbol{s}$.

The functional samples are generated using the R package `RandomFields` [Schlather et al., 2015]. Fig. 4 shows representative realizations from models M0–M3. Model M1 differs from M0 through a magnitude shift over a localized 40° latitude band centered at a random latitude; M2 differs from M0 through a change in covariance structure in the regions below latitude −50° and above latitude 50°; M3 differs from M0 through a shape perturbation over the entire domain. Models M1–M3 are particularly challenging to distinguish from M0. In particular, M1 differs from M0 only through a small magnitude shift, whereas M2 and M3 exhibit covariance and shape differences that are known to be difficult for integrated functional depths to detect and are commonly referred to as hard-to-detect outliers [see, e.g., Arribas-Gil and Romo, 2014, Ieva and Paganoni, 2020].

We consider the proposed VD with the univariate Simplicial depth [Liu, 1990] as D and a Voronoi tessellation associated with a uniform Delaunay triangulation $\mathcal{T}$ of S with $K = 3509$ nodes. The implementation is based on

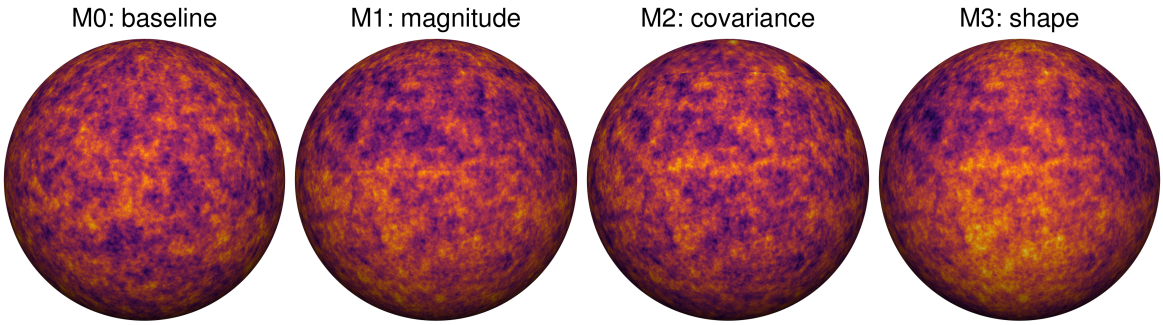

Fig. 4: Representative realizations from models M0–M3.

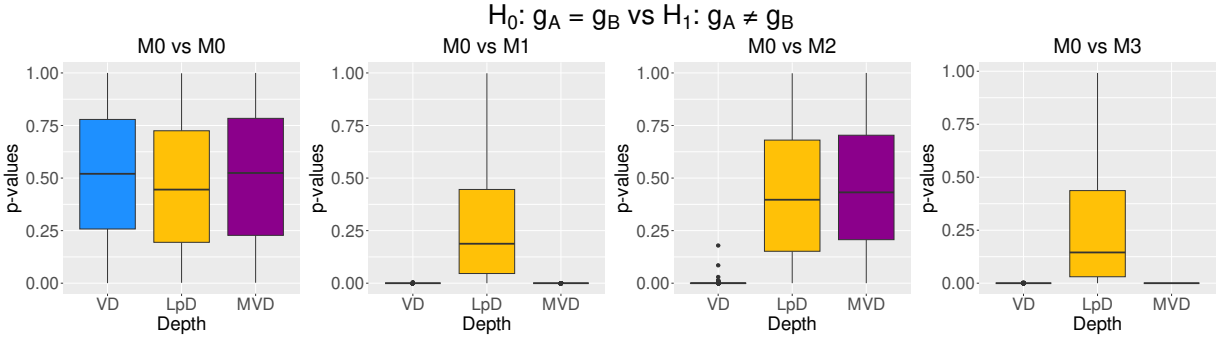

Fig. 5: Boxplots of Wilcoxon rank test p-values [Liu, 1990] when the first sample is generated under M0 and the second sample is generated under M0 (first panel), M1 (second panel), M2 (third panel), and M3 (fourth panel). Results for the proposed Voronoi Depth (VD), L_p depth (LpD), and Modified Volume Depth (MVD) are shown in blue, yellow, and purple, respectively.

the R/C++ library `fdaPDE` [Arnone et al., 2025], and is available at `https://github.com/MicheleCavazzutti/fdaPDE-R-depth`. We compare the proposed approach with two classical alternatives: the L_p depth (LpD) of Zuo and Serfling [2000], implemented in the R package `depthProc` [Kosiorowski and Zawadzki, 2019], and the Modified Volume Depth (MVD) of Genton et al. [2014], implemented in the R package `depthTests` [López-Pintado and Wrobel, 2017]. Neither method is designed for functional data on multidimensional supports: LpD treats observations as multivariate data, whereas MVD treats them as functional data on a one-dimensional domain obtained by vectorizing the support along one coordinate direction.

We assess the ability of the proposed depths to discriminate between populations using the depth-based Wilcoxon rank test of Liu [1990], later adopted in the functional depth literature by, among others, López-Pintado and Romo [2009, 2011] and Ieva and Paganoni [2013].

We simulate two functional samples, $\{X_i^{\mathrm{A}}\}_{i\in\{1,\dots,n_{\mathrm{A}}\}} \sim g_{\mathrm{A}}$ and $\{X_i^{\mathrm{B}}\}_{i\in\{1,\dots,n_{\mathrm{B}}\}} \sim g_{\mathrm{B}}$ with $n_{\mathrm{A}} = 100$ and $n_{\mathrm{B}} = 50$. To enable the application of LpD and MVD, which require a common observation grid across all statistical units, each function is evaluated on a common set of locations $\{\boldsymbol{s}_1, \dots, \boldsymbol{s}_m\}$ corresponding to a regular longitude-latitude lattice of $2^\circ \times 2^\circ$ size. This setting mimics the observational pattern of the application described in Section 6.

We consider the hypothesis test

$$\mathrm{H}_0 : g_{\mathrm{A}} = g_{\mathrm{B}} \qquad vs \qquad \mathrm{H}_1 : g_{\mathrm{A}} \neq g_{\mathrm{B}}.$$

We take as reference sample $x_1, \dots, x_{n_{\mathrm{A}}} \sim g_{\mathrm{A}} \cong X^{\mathrm{M0}}$, that is, distributed according to M0, and consider four different choices for the distribution g_{B}. In the first case, we perform the test with $g_{\mathrm{B}} \cong X^{\mathrm{M0}}$, so that there is no difference between the two populations. We then consider the cases $g_{\mathrm{B}} \cong X^{\mathrm{M1}}$, $g_{\mathrm{B}} \cong X^{\mathrm{M2}}$, and $g_{\mathrm{B}} \cong X^{\mathrm{M3}}$.

Fig. 5 presents boxplots of the p-values of the depth-based Wilcoxon rank test computed using VD, LpD, and MVD over 500 simulation replications. The left panel corresponds to the setting in which both samples are generated under M0, so that the null hypothesis holds. In this case, all methods correctly yield high p-values, indicating the absence of spurious differences between the two populations. The remaining panels correspond to settings in which the second sample is generated under M1, M2, and M3, respectively. When the second sample is generated under M1 or M3 (second and fourth panels), LpD yields high p-values, incorrectly failing to reject the null hypothesis, whereas the functional methods VD and MVD correctly produce low p-values. When the second sample is generated under M2 (third panel), only the proposed VD successfully distinguishes

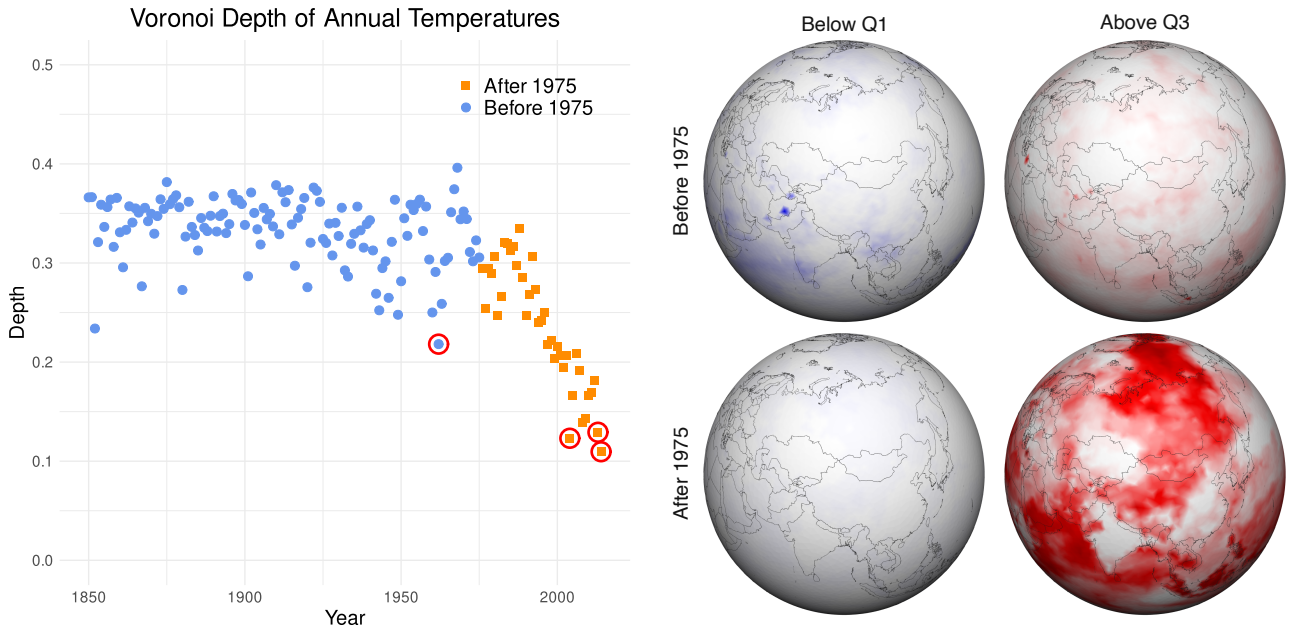

Fig. 6: Left panel: Voronoi Depth values for annual mean temperature fields over the period 1850–2014, computed with respect to the 1850–1975 reference period. Red-circled points correspond to years exceeding the boxplot fences. Right panel: for each cell of $\mathcal{V}$, the percentage of annual temperature fields lying below the first quartile (Q1) or above the third quartile (Q3), before and after 1975. Blue: below Q1; red: above Q3.

the two distributions. This occurs because MVD is based on the direct aggregation of the univariate depth contributions at each location and does not account for the dependence structure among neighboring locations. As a result, it fails to capture the covariance differences between M0 and M2, which are instead detected by VD. These results highlight the advantages of the proposed method, which is the only depth able to correctly distinguish the two populations in all the scenarios considered.

6 Analysis of Earth Surface Temperatures

The CESM2-LENS2 dataset [Rodgers et al., 2021] provides an open-access collection of climate model simulations for the study of internal variability and climate change. We analyze annual average surface temperatures (1850–2014) under CMIP6 historical radiative forcing, an environmental variable that has recently been extensively studied using stochastic generators [Jeong et al., 2019, Song et al., 2024]. Temperature fields are observed on a $0.9375° \times 1.25°$ (latitude $\times$ longitude) grid that is irregularly spaced over the Earth's surface, with denser sampling near the poles and sparser sampling near the equator; see Fig. 1. Existing depth methods, such as LpD and MVD (Section 5), would overweight high-latitude regions and underweight equatorial regions. In contrast, the proposed VD, combined with a regular Voronoi tessellation, assigns approximately uniform surface-area weights, yielding depth evaluations that are robust to irregular spatial sampling.

Consistent with documented global warming patterns, annual temperature fields in recent decades tend to exhibit higher temperatures and greater spatial heterogeneity. As a result, their depth is expected to decrease progressively, reflecting an increasing departure from historical variability. To formally assess this shift, we use the period 1850–1975 as a baseline, in line with studies identifying 1975 as a structural breakpoint in global temperature evolution [Tomé and Miranda, 2004, Werner et al., 2015]. We then perform a depth-based Wilcoxon rank test [Liu, 1990] to compare temperature patterns before and after 1975, using the years 1850–1975 as the reference population. The resulting p-value ($< 10^{-16}$) confirms a significant difference between the two periods.

To further characterize this change, the left panel of Fig. 6 displays the temporal evolution of the VD, computed with respect to the reference population, i.e., $\mathrm{VD}(x, P_{1850-1975})$, where $P_{1850-1975}$ denotes the distribution of annual temperature fields during the reference period. The depth begins to decline in the mid-1960s and continues decreasing over subsequent decades, indicating that temperature fields become increasingly extreme over time. We also compute a functional boxplot for the reference period, defining the central 50% envelope, the first and third quartiles (Q1 and Q3), and the boxplot fences [Genton et al., 2014]. Within the reference period, only the year 1963 crosses the boxplot fences and is therefore classified as an outlier; this corresponds to an anomalously cold year. When post-1975 fields are compared with this reference envelope, the years 2004, 2013, and 2014 cross the upper fence, indicating warmer patterns relative to the historical baseline. Finally, to

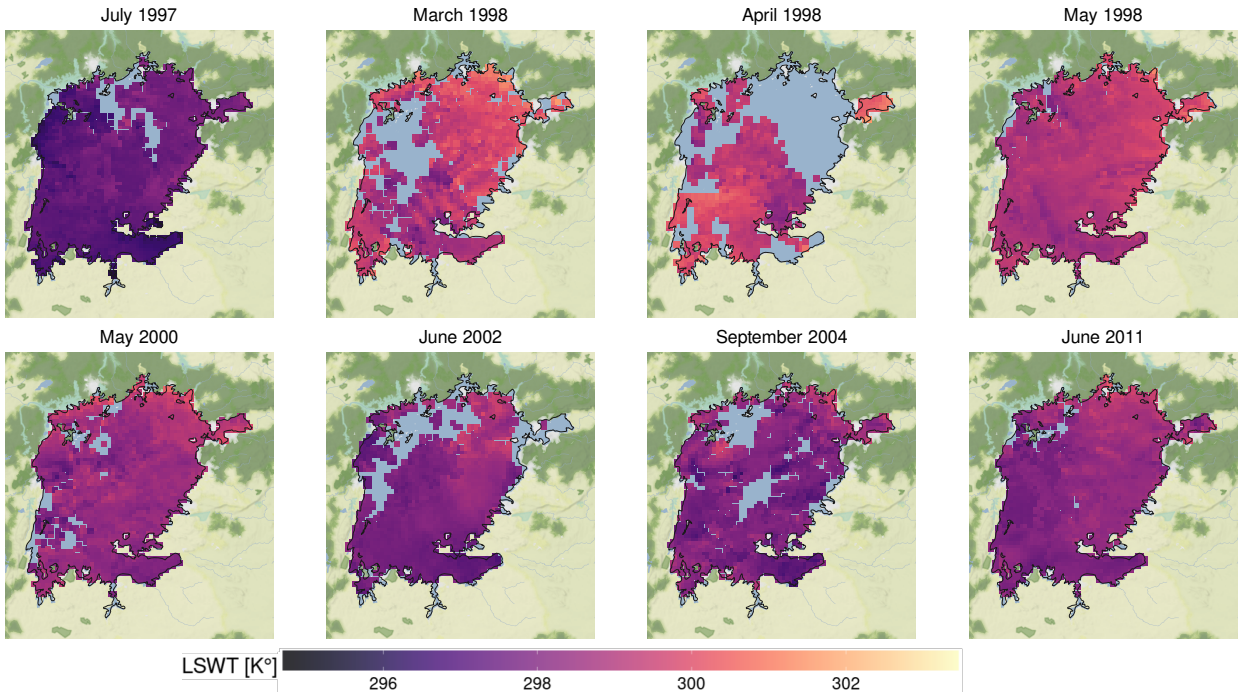

Fig. 7: Representative monthly Lake Victoria LSWT fields (K°).

examine the spatial expression of these deviations, we compute, for each $\boldsymbol{\xi}_k \in \mathcal{V}$, the proportion of years falling below Q1 or above Q3 (namely, belonging to the hypograph of Q1 or the epigraph of Q3) before and after 1975; see the right panel of Fig. 6. After 1975, exceedances occur almost exclusively above Q3 and reveal a strongly heterogeneous geographical warming pattern.

7 Analysis of Lake Water Surface Temperatures

As a second illustration of the proposed methodology, we consider Lake Surface Water Temperature (LSWT) over Lake Victoria in East Africa. LSWT is recognized as an essential climate variable and provides key information on hydrological and biogeochemical processes. The ARC-Lake database [MacCallum and Merchant, 2011] provides satellite-derived LSWT measurements on a $0.05° \times 0.05°$ grid from June 1995 to March 2012, yielding 202 monthly observations. Due to sensor limitations and cloud cover, the data exhibit substantial missingness (45.2%) with complex spatio-temporal patterns; see Fig. 7.

For this dataset, no clear long-term temporal trend is evident. Our objective is instead to characterize variability and identify anomalous temperature patterns. To this end, we construct a functional boxplot based on the proposed POVD. Unlike the surface boxplot of Genton et al. [2014], which requires fully observed functional surfaces, POVD enables the definition of central envelopes and outlier regions even under partial observability.

Fig. 8 displays the median and the central 50% envelope. The median corresponds to June 2011 (also shown in the bottom-right panel of Fig. 7), while the first and third quartiles define, cell by cell, the pointwise bounds of the central region. This representation highlights the main spatial structure of LSWT: a persistent warm gradient from the south-west to the north-east, together with more pronounced extremes in the enclosed eastern bays, where water circulation is restricted. These patterns reflect both the influence of the lake's geomorphology and the ability of POVD to handle irregular spatial supports.

We then compare each monthly field with the central envelope. The months displayed in the top row of Fig. 7 exceed the boxplot fences and are therefore identified as outliers. The functional boxplot of Sun and Genton [2011] is primarily designed to detect magnitude outliers and may be less sensitive to shape and covariance outliers. Focusing on magnitude outliers, March–May 1998 form a consecutive outlying episode, coinciding with a strong El Niño event that raised the lake level by approximately one meter and altered its thermal structure. This example illustrates how the proposed depth can reveal and help interpret anomalous functional behavior over complex two-dimensional domains, even in the presence of missing observations.

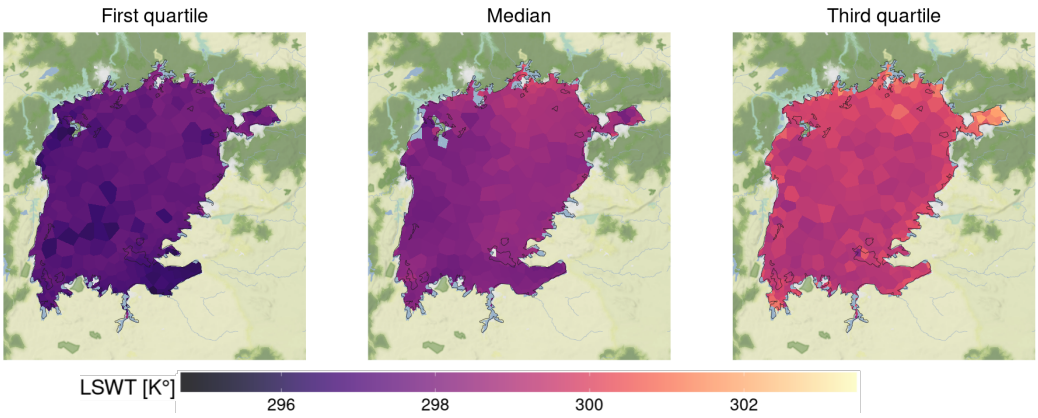

Fig. 8: Surface boxplot of the LSWT temperatures over Lake Victoria, constructed based on the proposed POVD. We report the median and the first and third quartiles.

8 Conclusion and future developments

In this manuscript, we extended the integrated functional depth to data defined on multidimensional supports with complex geometries. The proposed approach accommodates discretely observed, irregularly sampled, and partially observed functional data without requiring common grids or missing-data reconstruction. The resulting depth is consistent, detects magnitude, covariance, and shape outliers, and remains robust under increasing levels of missingness.

Future research could extend the proposed depth to vector-valued functions defined on multidimensional supports, as in Claeskens et al. [2014], Ieva and Paganoni [2020], Dai and Genton [2019] for one-dimensional domains. Another promising direction is the extension of Directional Outlyingness [Dai and Genton, 2019], which is closely related to integrated depth, to multidimensional supports in order to enhance the detection of shape outliers.

Acknowledgments

M. Cavazzutti, A. Palummo and L.M. Sangalli acknowledge Ministero dell'Università e della Ricerca, Dipartimento d'Eccellenza 2022–2027, Dipartimento di Matematica, Politecnico di Milano. M. Cavazzutti acknowledges King Abdullah University of Science and Technology for financial support during his visiting period. A. Palummo acknowledges funding by the European Union - NextGenerationEU program. L.M. Sangalli acknowledges the PRIN 2022 project CoEnv- Complex Environmental Data and Modeling (CUP 2022E3RY23), funded by the European Union - NextGenerationEU program, and by the Ministero dell'Università e della Ricerca.

ORCID

Michele Cavazzutti, https://orcid.org/0009-0007-7876-3357
Alessandro Palummo, https://orcid.org/0009-0002-0433-4959
Eleonora Arnone, https://orcid.org/0000-0002-8712-3489
Ying Sun, https://orcid.org/0000-0001-6703-4270
Marc G. Genton, https://orcid.org/0000-0001-6467-2998
Laura M. Sangalli, https://orcid.org/0000-0002-4951-9239

Supporting information

Additional supporting information can be found online in the Supplementary Material section at the end of this article.

References

E. Arnone, L. Negri, F. Panzica, and L. M. Sangalli. Analyzing data in complicated 3d domains: Smoothing, semiparametric regression, and functional principal component analysis. *Biometrics*, 2023. doi: https://doi.org/10.1111/biom.13845.

E. Arnone, A. Clemente, L. M. Sangalli, E. Lila, J. Ramsay, and L. Formaggia. *fdaPDE: Physics-Informed Spatial and Functional Data Analysis*, 2025. URL https://CRAN.R-project.org/package=fdaPDE. R package version 1.1-21.

A. Arribas-Gil and J. Romo. Shape outlier detection and visualization for functional data: the outliergram. *Biostatistics*, 15(4):603–619, 03 2014. ISSN 1465-4644.

P. Billingsley. *Convergence of Probability Measures*. John Wiley & Sons, New York, 1999.

A. Chakraborty and P. Chaudhuri. On data depth in infinite dimensional spaces. *Annals of the Institute of Statistical Mathematics*, 66(2):303–324, 2014.

G. Claeskens, M. Hubert, L. Slaets, and K. Vakili. Multivariate functional halfspace depth. *Journal of the American Statistical Association*, 109(505):411–423, 2014.

Copernicus Programme. Europe's earth observation programme, 2014. URL https://www.copernicus.eu.

A. Cuevas, M. Febrero, and R. Fraiman. Robust estimation and classification for functional data via projection-based depth notions. *Computational Statistics*, 22(3):481–496, 2007.

W. Dai and M. G. Genton. Functional boxplots for multivariate curves. *Stat*, 7(1), 2019. doi: https://doi.org/10.1002/sta4.190.

M. De Berg. *Computational Geometry: Algorithms and Applications*. Springer Science & Business Media, 2000.

A. Delaigle and P. Hall. Classification using censored functional data. *Journal of the American Statistical Association*, 108(504):1269–1283, 2013.

A. Elías and S. Nagy. Statistical properties of partially observed integrated functional depths. *TEST*, 34: 125–150, 2025. ISSN 1863-8260.

A. Elías, R. Jiménez, A. M. Paganoni, and L. M. Sangalli. Integrated depths for partially observed functional data. *Journal of Computational and Graphical Statistics*, 32(2):341–352, 2023. doi: 10.1080/10618600.2022.2070171.

R. Fraiman and G. Muniz. Trimmed means for functional data. *TEST*, 10(2):419–440, 2001.

M. G. Genton, C. Johnson, K. Potter, G. Stenchikov, and Y. Sun. Surface boxplots. *Stat*, 3(1):1–11, 2014. doi: https://doi.org/10.1002/sta4.39.

I. Gijbels and S. Nagy. On a general definition of depth for functional data. *Statistical Science*, 32(4):630–639, 2017.

Ø. Hjelle and M. Dæhlen. *Triangulations and Applications*. Springer, 1 edition, 2006.

R. J. Hyndman and H. L. Shang. Rainbow plots, bagplots, and boxplots for functional data. *Journal of Computational and Graphical Statistics*, 19(1):29–45, 2010.

F. Ieva and A. M. Paganoni. Depth measures for multivariate functional data. *Communications in Statistics - Theory and Methods*, 42(7):1265–1276, 2013.

F. Ieva and A. M. Paganoni. Component-wise outlier detection methods for robustifying multivariate functional samples. *Statistical Papers*, 61(2):595–614, 2020.

G. M. James and T. J. Hastie. Functional linear discriminant analysis for irregularly sampled curves. *Journal of the Royal Statistical Society Series B: Statistical Methodology*, 63(3):533–550, 2001.

J. Jeong, Y. Yan, S. Castruccio, and M. G. Genton. A stochastic generator of global monthly wind energy with Tukey g-and-h autoregressive processes. *Statistica Sinica*, 29(3):1105–1126, 2019. ISSN 10170405, 19968507. URL https://www.jstor.org/stable/26705995.

JPL MUR MEaSUREs Project. GHRSST Level 4 MUR Global Foundation Sea Surface Temperature Analysis. Ver. 4.1. PO.DAAC, CA, USA. https://podaac.jpl.nasa.gov/dataset/MUR-JPL-L4-GLOB-v4.1, 2015.

A. Kneip and D. Liebl. On the optimal reconstruction of partially observed functional data. *The Annals of Statistics*, 48(3):1692–1717, 2020.

D. Kosiorowski and Z. Zawadzki. DepthProc An R Package for Robust Exploration of Multidimensional Economic Phenomena. *arXiv preprint arXiv:1408.4542*, 2019. URL https://arxiv.org/abs/1408.4542.

D. Kraus. Components and completion of partially observed functional data. *Journal of the Royal Statistical Society Series B: Statistical Methodology*, 77(4):777–801, 09 2014. ISSN 1369-7412.

J. Li, J. A. Cuesta-Albertos, and R. Y. Liu. Dd-classifier: Nonparametric classification procedure based on dd-plot. *Journal of the American Statistical Association*, 107(498):737–753, 2012.

Z. Lin, J.-L. Wang, and Q. Zhong. Basis expansions for functional snippets. *Biometrika*, 108(3):709–726, 2021.

R. Y. Liu. On a notion of data depth based on random simplices. *The Annals of Statistics*, 18(1):405–414, 1990. ISSN 00905364.

S. López-Pintado and J. Romo. Depth-based classification for functional data. *DIMACS Series in Discrete Mathematics and Theoretical Computer Science*, 72:103, 2006.

S. López-Pintado and J. Romo. On the concept of depth for functional data. *Journal of the American Statistical Association*, 104(486):718–734, 2009.

S. López-Pintado and J. Romo. A half-region depth for functional data. *Computational Statistics & Data Analysis*, 55(4):1679–1695, 2011. ISSN 0167-9473.

S. López-Pintado and J. Wrobel. Robust non-parametric tests for imaging data based on data depth. *Stat*, 6 (1):405–419, 2017.

S. MacCallum and C. Merchant. Arc-lake v1.1-per-lake, 1995–2009, 2011. URL https://doi.org/10.7488/ds/159.

I. Molchanov and F. Molinari. *Random Sets in Econometrics*. Econometric Society Monographs. Cambridge University Press, 2018.

K. Mosler. *Depth Statistics*, pages 17–34. Springer Berlin Heidelberg, Berlin, Heidelberg, 2013. ISBN 978-3-642-35494-6.

S. Nagy, I. Gijbels, and D. Hlubinka. Weak convergence of discretely observed functional data with applications. *Journal of Multivariate Analysis*, 146:46–62, 2016a. ISSN 0047-259X.

S. Nagy, I. Gijbels, M. Omelka, and D. Hlubinka. Integrated depth for functional data: statistical properties and consistency. *ESAIM: PS*, 20:95–130, 2016b.

N. N. Narisetty and V. N. Nair. Extremal depth for functional data and applications. *Journal of the American Statistical Association*, 111(516):1705–1714, 2016.

A. Nieto-Reyes and H. Battey. A topologically valid definition of depth for functional data. *Statistical Science*, 31(1):61–79, 2016.

H. Ombao, M. Lindquist, W. Thompson, and J. Aston. *Handbook of neuroimaging data analysis*. Chapman and Hall/CRC, 2016.

A. B. Owen. *Monte Carlo Theory, Methods and Examples*. https://artowen.su.domains/mc/, 2013.

Z. Qu and M. G. Genton. Sparse functional boxplots for multivariate curves. *Journal of Computational and Graphical Statistics*, 31(4):976–989, 2022.

Z. Qu, W. Dai, C. Euan, Y. Sun, and M. G. Genton. Exploratory functional data analysis (with discussion). *TEST*, 34:459–482, 2025. ISSN 1863-8260. doi: 10.1007/s11749-024-00952-8.

A. Quarteroni and A. Valli. *Domain Decomposition Methods for Partial Differential Equations*. Oxford University Press, 1 edition, 1999. Oxford Academic.

K. B. Rodgers, S. S. Lee, N. Rosenbloom, A. Timmermann, G. Danabasoglu, C. Deser, J. Edwards, J. E. Kim, I. R. Simpson, K. Stein, M. F. Stuecker, R. Yamaguchi, T. Bódai, E. S. Chung, L. Huang, W. M. Kim, J. F. Lamarque, D. L. Lombardozzi, W. R. Wieder, and S. G. Yeager. Ubiquity of human-induced changes in climate variability. *Earth System Dynamics*, 12(4):1393–1411, 2021. ISSN 2190-4979. Publisher Copyright: © 2021 Keith B. Rodgers et al.

M. Schlather, A. Malinowski, P. J. Menck, M. Oesting, and K. Strokorb. Analysis, simulation and prediction of multivariate random fields with package RandomFields. *Journal of Statistical Software*, 63(8):1–25, 2015.

R. Serfling and U. Wijesuriya. Depth-based nonparametric description of functional data, with emphasis on use of spatial depth. *Computational Statistics & Data Analysis*, 105:24–45, 2017. ISSN 0167-9473.

C. Sguera and S. López-Pintado. A notion of depth for sparse functional data. *Test*, 30(3):630–649, 2021.

Y. Song, Z. Khalid, and M. G. Genton. Efficient stochastic generators with spherical harmonic transformation for high-resolution global climate simulations from CESM2-LENS2. *Journal of the American Statistical Association*, 119(548):2493–2507, 2024. doi: 10.1080/01621459.2024.2360666.

J. Stewart. *Calculus*. Cengage Learning, 2015. ISBN 9781305480513.

Y. Sun and M. G. Genton. Functional boxplots. *Journal of Computational and Graphical Statistics*, 20(2): 316–334, 2011. doi: 10.1198/jcgs.2011.09224.

Y. Sun and M. G. Genton. Adjusted functional boxplots for spatio-temporal data visualization and outlier detection. *Environmetrics*, 23(1):54–64, 2012. doi: https://doi.org/10.1002/env.1136.

A. R. Tomé and P. M. A. Miranda. Piecewise linear fitting and trend changing points of climate parameters. *Geophysical Research Letters*, 31(2), 2004.

J. W. Tukey. Mathematics and picturing data. In R. D. James, editor, *Proceedings of the 1974 International Congress of Mathematicians*, volume 2, pages 523–531. Canadian Mathematical Congress, Vancouver, 1975.

R. Werner, D. Valev, D. Danov, and V. Guineva. Study of structural break points in global and hemispheric temperature series by piecewise regression. *Advances in Space Research*, 56(11):2323–2334, 2015. ISSN 0273-1177.

Y. Zuo and R. Serfling. General notions of statistical depth function. *The Annals of Statistics*, 28(2):461–482, 2000. ISSN 00905364.

Supplementary material to "Voronoi depth for functional data over non-convex multidimensional supports"

M. Cavazzutti[1], **A. Palummo**[1], **E. Arnone**[2], **Y. Sun**[3], **M. G. Genton**[3], and **L. M. Sangalli**[*1]

[1]MOX - Dept. of Mathematics, Politecnico di Milano, Milan, Italy
[2]Dept. of Management, University of Torino, Turin, Italy
[3]Statistics Program, King Abdullah University of Science and Technology, Thuwal, Saudi Arabia

4 November 2026

Abstract

This supplementary material provides additional results supporting the paper "Voronoi depth for functional data over non-convex multidimensional supports".

1 Definitions and assumptions used in the main manuscript

For completeness, we recall the definitions and assumptions used throughout the main manuscript.

We first recall properties (D1)–(D7) of Nagy et al. [2016], which are assumed to hold for the univariate depth integrand used in the definition of the Voronoi depth.

In what follows, let $\mathrm{Q} \in \mathcal{P}(\mathbb{R}^{K^\star})$ for $K^\star \in \mathbb{N}$, where $\mathcal{P}(\mathbb{R}^{K^\star})$ denotes the collection of all probability measures on $\mathbb{R}^{K^\star}$. Let also U be a random vector taking values in $\mathbb{R}^{K^\star}$, and let Q_U denote the probability measure associated with U. We recall that each one-dimensional distribution $\mathrm{Q} \in \mathcal{P}(\mathbb{R})$ having a median $u^* \in \mathbb{R}$ is halfspace symmetric around u^*. Note, however, that, particularly in one dimension, the center of halfspace symmetry need not be unique when the support of Q is disconnected. The properties required for a depth function to serve as a well-defined integrand of an integrated depth are listed below.

D1: *Affine invariance:* For any non-singular matrix $A \in \mathbb{R}^{K^\star \times K^\star}$, any $b, u \in \mathbb{R}^{K^\star}$, and any random vector U

$$D\left(u; \mathrm{Q}_U\right) = D\left(Au + b; \mathrm{Q}_{AU+b}\right).$$

D2: *Maximality at center:* If the distribution of U is halfspace symmetric around $u^* \in \mathbb{R}^{K^\star}$, then u^* maximizes $D(u; \mathrm{Q}_U)$.

D3: *Quasi-concavity as a function of u:* The level set $\{u : D(u; \mathrm{Q}) \geq c\}$ is convex for each $c \in \mathbb{R}$.

D4: *Vanishing at infinity:* $D(u; \mathrm{Q}) \xrightarrow[\|u\|_{\mathbb{R}^{K^\star}} \to \infty]{} 0$, where $\|u\|_{\mathbb{R}^{K^\star}}$ stands for the Euclidean norm on $\mathbb{R}^{K^\star}$.

D5: *Upper semicontinuity of D as a function of u:* For all $u \in \mathbb{R}^{K^\star}$ and $u_\nu \xrightarrow[\nu \to \infty]{} u$

$$\limsup_{\nu \to \infty} D\left(u_\nu; \mathrm{Q}\right) \leq D\left(u; \mathrm{Q}\right).$$

D6: *Weak continuity of D as a functional of Q:* For all $\mathrm{Q}_\nu \xrightarrow[\nu \to \infty]{w} \mathrm{Q}$

$$\sup_{u \in \mathbb{R}^K} \left|D\left(u; \mathrm{Q}_\nu\right) - D\left(u; \mathrm{Q}\right)\right| \xrightarrow[\nu \to \infty]{} 0.$$

D7: *Measurability*: The mapping

$$D : \mathbb{R}^{K^\star} \times \mathcal{P}(\mathbb{R}^{K^\star}) \to [0, 1]$$

is jointly Borel measurable and $D(\cdot, Q) \not\equiv 0$ for all $Q \in \mathcal{P}(\mathbb{R}^{K^\star})$.

*Correspondence: Laura.sangalli@polimi.it

Note that, in the main manuscript, these properties are required to hold for $K^\star = 1$. In addition to the aforementioned properties, we also refer to the notions of *strong consistency*, *uniform consistency*, and *weak continuity* of the univariate depth D, which are assumed in several propositions and theorems of the main manuscript. These notions are formally defined in Elías and Nagy [2025] and are recalled here for completeness. Let $R \in \mathcal{P}(\mathbb{R}^{K^\star})$ be a probability distribution. Given a sample Y_i, $i = 1, \ldots, n$, let $R_n := \sum_{i=1}^{n} Y_i \delta_{Y_i}$ denote the corresponding empirical estimate of R obtained from the sample.

C1: *Strong consistency*: the depth $D : \mathbb{R}^{K^\star} \times \mathcal{P}(\mathbb{R}^{K^\star}) \to [0, 1]$ is strong consistent if

$$D(u; R_n) \xrightarrow[n\to\infty]{a.s.} D(u; R), \quad \forall u \in \mathbb{R},$$

for all Borel probability measures R in $\mathcal{P}(\mathbb{R}^{K^\star})$.

C2: *Uniform consistency*: the depth D is uniform consistent if

$$\sup_{u \in \mathbb{R}^{K^\star}} |D(u; R_n) - D(u; R)| \xrightarrow[n\to\infty]{a.s.} 0,$$

for all Borel probability measures in $\mathcal{P}(\mathbb{R}^{K^\star})$.

C3: *Weak continuity*: the depth D is weakly continuous if

$$\sup_{u \in \mathbb{R}^{K^\star}} |D(u; R_\gamma) - D(u; R)| \xrightarrow[\gamma\to\infty]{a.s.} 0,$$

for all sequences $\{R_\gamma\}_{\gamma=1}^{\infty}$ of Borel probability measures R in $\mathcal{P}(\mathbb{R}^{K^\star})$ that converge weakly to R, were R is any measure from the collection of marginal distributions $\{P_{\boldsymbol{s}}\}_{\boldsymbol{s}\in S}$ of P.

2 Simulation study: Partial Observability

In this simulation study, we assess the robustness of the proposed depth under partial observability. To this end, we first generate a fully observed sample on the same common locations used in Simulation 1 and compute the proposed Partially Observed Voronoi Depth (POVD) and the competing depths. We then partition the spherical surface into $K = 28$ non-overlapping regions of size $60° \times 60°$. For each statistical unit, a subset of these regions is randomly masked, and only observations in the remaining regions are retained. We consider different levels of observability, ranging from 100% to 50% in decrements of 5%. For each setting, we compute the depths from the partially observed sample and calculate the Spearman correlation between the depth computed from the fully observed data and that computed from the partially observed data.

The entire procedure is repeated under two settings, each with $n = 50$. In the first setting, $\{X_i\}_{i\in 1,\ldots,n}$ is generated entirely under M0. In the second, 90% of the sample is generated under M0 and the remaining 10% under M2, thereby introducing covariance outliers. The experiment is replicated 500 times.

The proposed POVD naturally accommodates partially observed data. In contrast, the competing methods, L_p depth (LpD) and Modified Volume Depth (MVD), require additional processing. We therefore consider two alternatives. In the first, the competing depths are computed using only the common domain, i.e., the locations at which all $n = 50$ functional observations are available, discarding locations where at least one observation is missing. In the second, the competing depths are computed after reconstructing the partially observed functions using DINEOF, a widely used spatial reconstruction method proposed by Beckers and Rixen [2003] and implemented in the package `sinkr` [Taylor, 2025]. To ensure the applicability of the common-domain approach, we arbitrarily require one $60° \times 60°$ region to be observed for all functions. Note, however, that neither POVD nor the competing depths computed from DINEOF-reconstructed data require the existence of a common domain.

Overall, we consider the following five methods:

- POVD: the proposed Partially Observed Voronoi Depth;
- LpD-CD: the L_p depth computed on the available common domain;
- MVD-CD: the Modified Volume Depth computed on the available common domain;
- LpD-DINEOF: the L_p depth computed on the DINEOF-reconstructed data;
- MVD-DINEOF: the Modified Volume Depth computed on the DINEOF-reconstructed data.

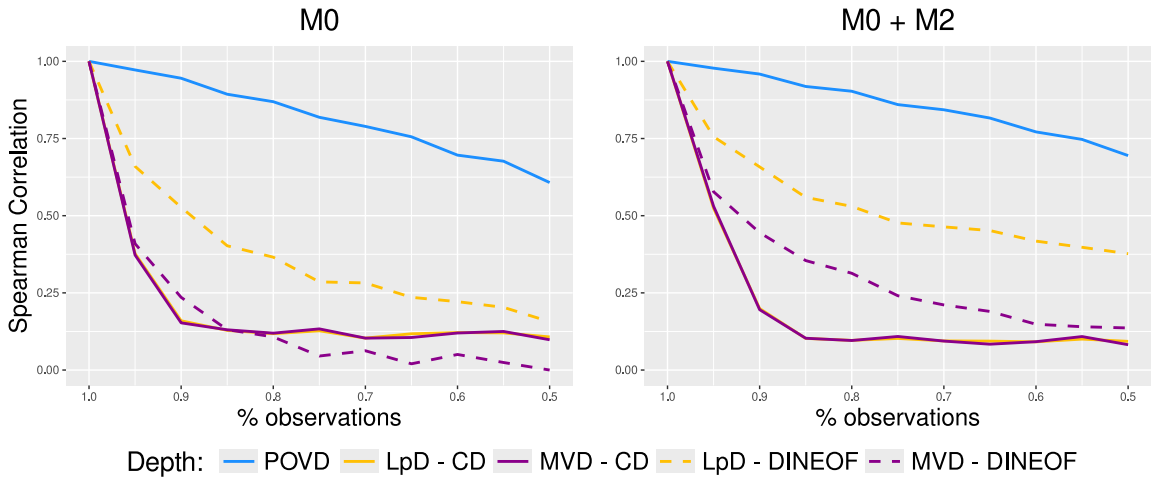

Fig. 1: Spearman correlation between the depth computed from fully observed data and the corresponding depth computed from partially observed data across different levels of observability. Left panel: fully observed sample generated under M0. Right panel: sample generated under a mixture of models M0 and M2. Correlations obtained using the proposed Partially Observed Voronoi Depth (POVD) are shown in light blue, those obtained using the L_p depth (LpD-CD and LpD-DINEOF) in yellow, and those obtained using the Modified Volume Depth (MVD-CD and MVD-DINEOF) in purple. For LpD and MVD, solid lines correspond to depths computed on the common domain (CD), whereas dashed lines correspond to depths computed on the DINEOF-reconstructed data.

Figure 1 displays the correlation curves for the two settings described above, namely when all functional data are generated under M0 and when they are generated from a mixture of models M0 and M2. The LpD and MVD methods computed on the common domain generally yield poorer results than their DINEOF-based counterparts, particularly in the M0+M2 setting, even at an observability level of 90%. In both settings, the proposed POVD outperforms all competing methods by a substantial margin. These results highlight the robustness and accuracy of the proposed depth under partial observability.

3 Simulation study: sensitivity to Voronoi tessellation refinement

In the main manuscript, the Voronoi tessellation is a user-defined parameter whose choice should reflect the spatial distribution of the phenomenon under study [De Berg, 2000]. The number of Voronoi seeds determines the resolution of the tessellation and may therefore affect the performance of the proposed depth. In this simulation study, we investigate this dependence by assessing how the ability of the proposed depth to discriminate between different populations varies with the number of Voronoi seeds.

We consider the proposed VD equipped with the univariate Simplicial depth [Liu, 1990] as D and four possible cases of Voronoi tessellations associated with uniform Delaunay triangulations $\mathcal{T}$ of S with $K = 862, 1602, 3509$ and 13969 nodes. The last case corresponds to a very fine tessellation, with a number of Voronoi seeds comparable to the number of measurement locations. This setting is of particular interest because, as the tessellation becomes increasingly refined, the proposed depth approaches a direct aggregation of local depth contributions, and its behavior is therefore expected to become closer to that of MVD. We simulate two functional samples, $\{X_i^{\mathrm{A}}\}_{i\in 1\ldots,n_{\mathrm{A}}} \sim g_{\mathrm{A}}$ and $\{X_i^{\mathrm{B}}\}_{i\in 1\ldots,n_{\mathrm{B}}} \sim g_{\mathrm{B}}$ with $n_{\mathrm{A}} = 100$ and $n_{\mathrm{B}} = 50$. The functional data are evaluated on the same measurement locations set as in Section 5 of the main manuscript, which mimics the observational pattern of the application described in Section 6.

We consider the hypothesis test

$$\mathrm{H}_0 : g_{\mathrm{A}} = g_{\mathrm{B}} \qquad vs \qquad \mathrm{H}_1 : g_{\mathrm{A}} \neq g_{\mathrm{B}}.$$

We take as reference sample $x_1, \ldots, x_{n_{\mathrm{A}}} \sim g_{\mathrm{A}} \widetilde{=} X^{\mathrm{M0}}$, and consider two alternatives for the distribution g_{B}. Specifically, we perform the test with $g_{\mathrm{B}} \widetilde{=} X^{\mathrm{M1}}$ and $g_{\mathrm{B}} \widetilde{=} X^{\mathrm{M2}}$.

Figure 2 presents boxplots of the p-values of the depth-based Wilcoxon rank test based on VD, obtained from 500 simulation replications using the four Voronoi tessellations considered. For both scenarios, VD yields low p-values when $K = 862$, 1602, or 3509. In the more challenging M2 setting, performance deteriorates only when $K = 13969$, corresponding to a very fine tessellation with a number of Voronoi seeds comparable to the number of measurement locations. As K increases, the Voronoi cells become smaller and the local averaging effect induced by the tessellation progressively weakens, bringing the behavior of VD closer to that of MVD.

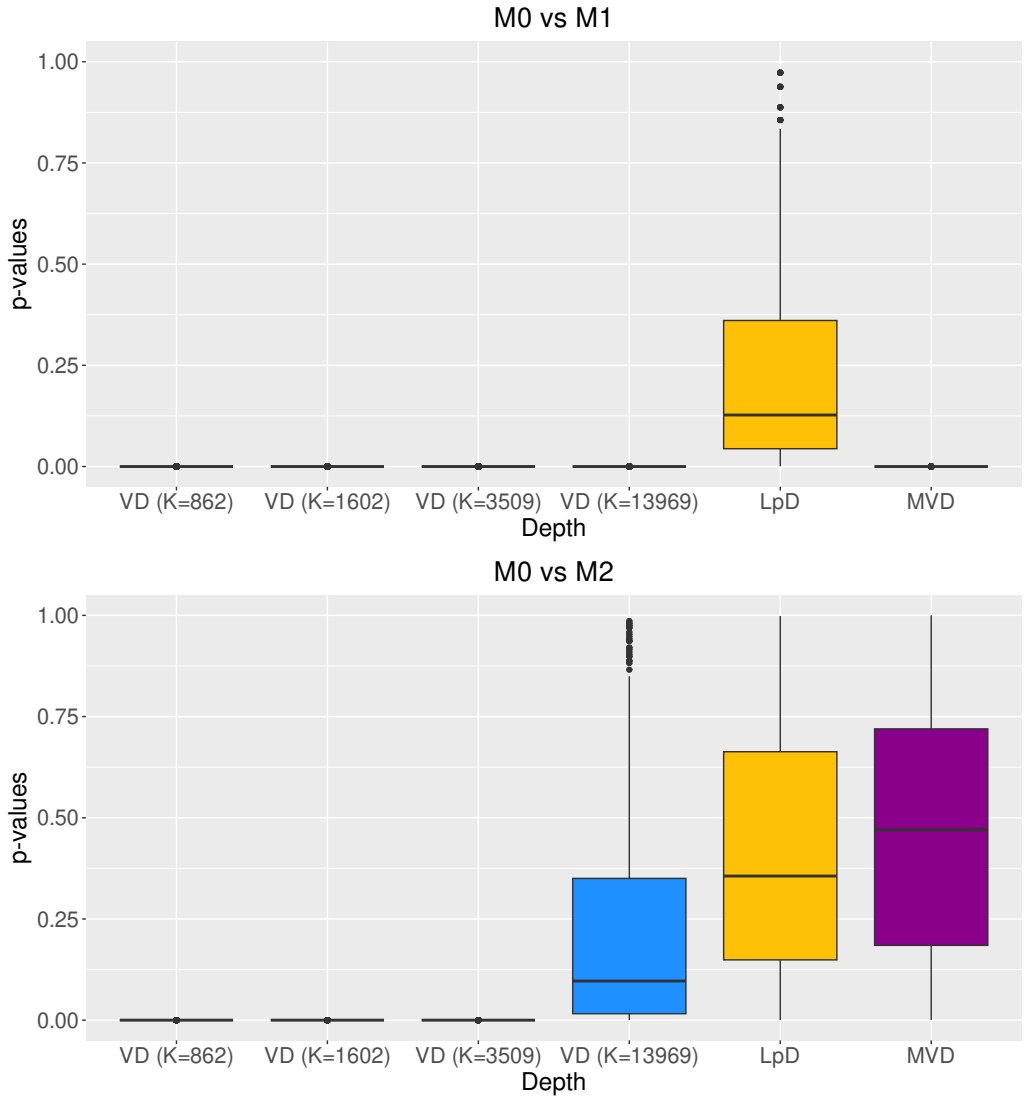

Fig. 2: Boxplots of the p-values of the Wilcoxon rank test [Liu, 1990] when the first sample is generated under M0 and the second sample is generated under M1 (upper panel) or M2 (lower panel). Boxplots corresponding to the proposed Voronoi Depth (VD) are shown in blue, those corresponding to the L_p depth (LpD) in yellow, and those corresponding to the Modified Volume Depth (MVD) in purple. The four VD boxplots correspond to Voronoi tessellations with increasing numbers of Voronoi seeds.

Nevertheless, VD remains more effective than the competing methods. Overall, the results suggest that the proposed depth is robust to the choice of K, provided that the tessellation is not excessively refined relative to the observation density.

References

J. M. Beckers and M. Rixen. EOF calculations and data filling from incomplete oceanographic datasets. *Journal of Atmospheric and Oceanic Technology*, 20(12):1839–1856, 2003.

M. De Berg. *Computational Geometry: Algorithms and Applications*. Springer Science & Business Media, 2000.

A. Elías and S. Nagy. Statistical properties of partially observed integrated functional depths. *TEST*, 34: 125–150, 2025. ISSN 1863-8260.

R. Y. Liu. On a notion of data depth based on random simplices. *The Annals of Statistics*, 18(1):405–414, 1990. ISSN 00905364.

S. Nagy, I. Gijbels, M. Omelka, and D. Hlubinka. Integrated depth for functional data: statistical properties and consistency. *ESAIM: PS*, 20:95–130, 2016.

M. Taylor. *sinkr: Collection of functions with emphasis in multivariate data analysis*, 2025. URL `https://github.com/marchtaylor/sinkr`. R package version 0.7.1.

MOX Technical Reports, last issues

Dipartimento di Matematica
Politecnico di Milano, Via Bonardi 9 - 20133 Milano (Italy)

82/2026 Botteghi, N.; Tomasetto, M.; Manzoni, A.
Reinforcement learning for control of partial differential equations

81/2026 Clemente, A.; Palummo, A.; Arnone, E.; Aston, J.A.D.; Panzica, F.; Sangalli, L.M.
Modeling spatio-temporal smoothness using nonlinear differential operators

80/2026 Botteghi, N; Glas, S; Brune, C
Deep Invertible Autoencoders for Dimensionality Reduction of Dynamical Systems

78/2026 Botteghi, N; Brook, O; Fasel, U; Califano, F
Interconnection and Damping Assignment Passivity-Based Control using Sparse Neural ODEs

79/2026 Vitullo, P.; Macaluso, C.; Gazzoni, S.; Cassanmagnago, A.; Dimola, N.; Possenti, L.; Zunino, P.
A computational model for phenotype-structured tumour dynamics with reduced microvascular oxygen and event-based radiotherapy

77/2026 Renzi, F.; Pagani, S.; Antonietti, P.F.; Vergara, C.
A Neural-Network Approach for the Stability of Loosely-Coupled FSI Simulations in Hemodynamics

75/2026 Botteghi, N; Tomasetto, M; Fasel, U; Braghin, F; Manzoni, A
HypeMARL: Multi-Agent Reinforcement Learning For High-Dimensional, Parametric, and Distributed Systems

76/2026 Pizzamiglio, S.M.; Pagani, S.; Regazzoni, F.
Learning PDE solution operators with variable initial conditions via Latent Dynamics Networks

74/2026 Brivio, S.; Franco, N. R.
Deep Symmetric Autoencoders from the Eckart-Young-Schmidt Perspective

73/2026 Corti, M.
A weighted polygonal discontinuous Galerkin method for hierarchically coupled reaction–diffusion systems with cubic interactions